JTTEE5 4:252-260


# Microstructure Evolution during Reactive Plasma Spraying of $MoSi_2$ with Methane

*X. Liang, E.J. Lavernia, J. Wolfenstine, and A. Sickinger*

**The mechanisms that govern microstructure evolution during reactive plasma spraying of $MoSi_2$ using 100% methane were investigated, with particular emphasis on the thermodynamics and kinetics of the relevant phase transformations and chemical reactions. The reactive plasma-sprayed $MoSi_2$ exhibited a dense, multilayered microstructure. In addition to the $MoSi_2$ matrix, significant amounts of $Mo_5Si_3$ and elemental carbon were observed, along with a small amount of SiC. Thermodynamic and kinetic analysis predicted a large volume fraction of $Mo_5Si_3$ and a small amount of SiC in the as-deposited reactive plasma-sprayed $MoSi_2$, in agreement with the experimental observations.**

## 1. Introduction

REACTIVE plasma spraying (RPS) is a single-step process that combines thermal plasma spraying, chemical reactions, and deposition to synthesize dispersion-strengthened materials or particulate-reinforced composites (Ref 1-3). During RPS, particulates of the matrix material are injected into a reactive environment. The combination of a high specific surface area of the fine particulates and the inherent high temperature of the thermal plasma provides favorable conditions for in-situ chemical reactions between the particulates and the reactive gas species. As a result, chemical reactions among reactive components may lead to the formation of a homogeneous distribution of fine carbide, oxide, and nitride reinforcements in the plasma-sprayed deposit, significantly improving mechanical properties of the matrix (Ref 1-3). This synthesis approach offers an opportunity for continuous control over composition and microstructure. In addition, inherent processing advantages allow RPS to produce bulk materials or surface coatings in a wide variety of geometries (Ref 4, 5). The synthesis of in-situ composites through RPS, however, is primarily limited to highly reactive metals, such as titanium and zirconium (Ref 1-3), to form oxide, nitride, or carbide reinforcements. The kinetics of the required chemical reactions for other materials usually hinders completeness of the reactions under the extremely heterogeneous conditions during thermal plasma spraying.

$MoSi_2$ has gained attention (Ref 6-8) as an elevated-temperature structural material because of its unique combination of physical characteristics. It has a moderate density of 6.31 g/cm$^3$, a high melting point of approximately 2030 °C, an excellent oxidation resistance that is essentially equivalent to that of the silicon-base structural ceramics (e.g., SiC and $Si_3N_4$), and a high modulus at elevated temperature (Ref 6-8). However, $MoSi_2$ exhibits poor creep resistance at elevated temperature and low fracture toughness at room temperature. Incorporation of ceramic reinforcements into the matrix of $MoSi_2$ significantly improves both high-temperature creep resistance and room-temperature fracture toughness (Ref 6, 7, 9).

Available techniques for synthesizing ceramic-reinforced $MoSi_2$ composites include powder metallurgy methods (e.g., pressure-assisted processing, reaction sintering, and mechanical alloying), solid-state reactions (e.g., self-propagating high-temperature synthesis, solid-state displacement reactions, and exothermic dispersion), and liquid-state reactions (Ref 6, 7). The mechanical properties of ceramic-reinforced $MoSi_2$ composites can also be improved through reactive thermal spraying, because the processed composites usually exhibit a dense matrix with uniform distribution of fine reinforcing particles. For example, low-pressure plasma spraying (LPPS) of $MoSi_2$ using methane as a carrier and reactive gas was investigated recently as a method to effectively incorporate carbon and carbide particles into $MoSi_2$ (Ref 10, 11). The existence of carbon and carbides dramatically increased high-temperature creep resistance and room-temperature fracture toughness, compared to LPPS $MoSi_2$ without methane (Ref 11, 12). The as-deposited RPS $MoSi_2$ material exhibited a complex microstructure that consisted of secondary phases, including $Mo_5Si_3$, $SiO_2$, SiC, and elemental carbon. It is interesting to note that a significant volume fraction of $Mo_5Si_3$ phase (~15 vol%) was frequently observed in the as-deposited RPS $MoSi_2$, but only a small volume fraction of SiC (<5 vol%) was present (Ref 11, 12). The formation of these secondary phases and the microstructure evolution during reactive plasma spraying of $MoSi_2$ have been generally associated with the highly heterogeneous thermal conditions provided by the arc plasma jet and the ensuing chemical reactions. However, a comprehensive analysis has not been attempted.

The objective of the present investigation is to provide insight into the mechanisms that govern microstructural evolution during reactive plasma spraying of $MoSi_2$ using methane as a reactive gas. Emphasis is placed on thermodynamic and kinetic analysis of the relevant phase transformations and chemical reactions occurring between $MoSi_2$ particulates and the reactive gas environment.

**Keywords:** $MoSi_2$, microstructure evolution, reactive plasma spraying

**X. Liang, E.J. Lavernia,** and **J. Wolfenstine,** Materials Science and Engineering, University of California, Irvine, CA 92717, USA; **A. Sickinger,** Sulzer Metco (Irvine) Inc., Irvine, CA 92714, USA.

## 2. Experimental Method

The $MoSi_2$ powders used in the present RPS experiment were obtained from CERAC (Milwaukee, WI). Particle sizes

**Table 1 Processing parameters for reactive plasma spraying of $MoSi_2$**

| Parameter | Value |
|---|---|
| Voltage, V | 44 |
| Current, A | 1400 |
| Primary arc gas (Ar), S/PM | 102 |
| Secondary arc gas ($H_2$), S/PM | 27 |
| Reactive gas ($CH_4$), S/PM | 27 |
| $MoSi_2$ powder feed rate, g/min | 50 |
| Atmosphere, Pa | $3 \times 10^4$ |
| Substrate distance, mm | 300 |
| Spray time, min | 58 |

ranged from 10 to 44 μm, with a purity of 99.5%. A 50 by 50 by 5 mm stainless steel plate was used as the substrate. The LPPS deposition experiment was conducted at Electro-Plasma Inc. (Irvine, CA). During RPS, the $MoSi_2$ powders were injected into an argon/hydrogen plasma gas jet using methane as a carrier gas. The methane gas subsequently became a reactive agent during plasma spraying. In addition, the positions of the plasma gun and substrate were controlled by a transverse motion in order to obtain a uniform thickness for the as-deposited material. The primary processing parameters used in the reactive plasma spraying of $MoSi_2$ are summarized in Table 1.

Following RPS processing, the as-deposited $MoSi_2$ was sectioned, polished, and etched using a reagent consisting of two parts $HNO_3$, one part HF, and five parts $H_2O$ (by volume). Optical microscopy examination was conducted using conventional and differential-interference contrast techniques. A transmission electron microscope (TEM) equipped with an 18° takeoff angle EDAX (energy-dispersive x-ray analysis) x-ray detector was also used to examine the microstructure of the as-deposited RSP $MoSi_2$. To prepare $MoSi_2$ TEM samples, the as-deposited material was first mechanically ground and polished to 100 μm; 3 mm diam disks were then sectioned from the ground and polished materials, and subsequently dimpled to about 20 μm. The dimpled samples were ion milled until suitable for TEM examination.

X-ray diffraction (XRD) studies for phase analysis were conducted on as-deposited RSP $MoSi_2$ using a diffractometer. X-ray diffraction patterns were obtained using $CuK_{\alpha 1}$ radiation ($\lambda$ = 1.5406 Å); measurements were scanned for 2θ diffraction angles from 20° to 80°, with a step interval of 0.05° and a time step of 1 s. An integrated software package, which includes a comprehensive database of XRD patterns for common organic, inorganic, and mineral materials, was used to control the measurement operations and to analyze the data.

## 3. Results

The as-deposited RPS $MoSi_2$ exhibits a microstructure that is typical for LPPS (Fig. 1). It is homogeneous and nearly fully dense, as indicated by a low porosity level of about 2 vol% determined by image analysis (Ref 13). In addition, the microstructure of as-deposited RPS $MoSi_2$ is characterized by a multilayered structure, which is similar to the results of other investigations (Ref 6, 11, 12, 14-19) of plasma-sprayed $MoSi_2$. Careful examination of the as-deposited materials revealed that

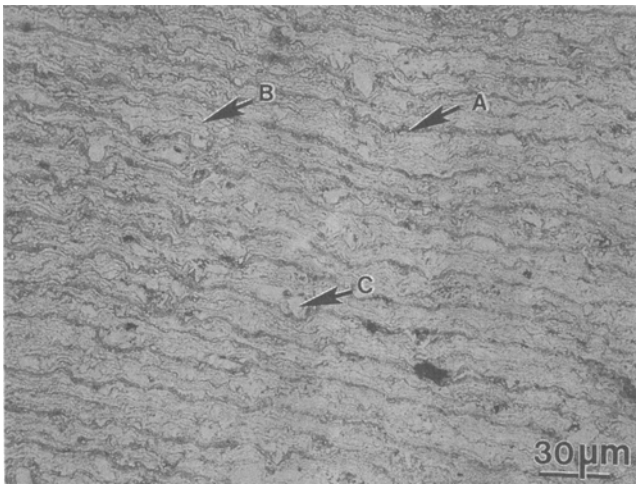


**Fig. 1** Micrograph of as-deposited $MoSi_2$, showing a multilayered structure. A, thick-layer boundary; B, thin-layer boundary; C, non-melted $MoSi_2$ particle

these layers can be further divided into two groups according to their thickness and morphology. The relatively thick layers, as indicated by boundaries marked A in Fig. 1, are parallel and have an average thickness of 13.3 μm. The formation of these thick-layer boundaries can be attributed to the intervals of transverse motion of the plasma spraying gun and the substrate. The relatively thin layers, as indicated by boundaries marked B in Fig. 1, have a splat morphology with an average thickness of 1.0 μm. The formation of the splat-layer microstructure suggested that the $MoSi_2$ particles experienced severe deformation during their impingement onto the substrate and that prior-droplet boundaries (i.e., solidified surface layer) existed before impingement. A fraction of $MoSi_2$ particles (10 to 20 vol%) exhibited a non-melted morphology (marked by C in Fig. 1), suggesting that these particles were incompletely melted or resolidified during plasma spraying.

X-ray diffraction patterns from the as-deposited RPS $MoSi_2$ (Fig. 2) revealed a complex phase constitution. For example, in addition to the strong tetragonal $MoSi_2$ peaks, strong peaks corresponding to tetragonal $Mo_5Si_3$ were observed, indicating the existence of a significant amount of $Mo_5Si_3$ phase in the deposited material. The $Mo_5Si_3$ phase in the as-deposited materials was determined to be approximately 13.5 vol% by Lawrynowicz et al. (Ref 11) using x-ray photoelectron spectroscopy. The diffraction patterns also suggested the existence of a significant amount of elemental carbon in the as-deposited RPS $MoSi_2$. The amount of elemental carbon was not determined. The presence of a significant volume fraction of $Mo_5Si_3$ phase and elemental carbon has also been reported previously for plasma-sprayed or RPS $MoSi_2$ (Ref 11, 12, 17, 18). X-ray diffraction did not reveal the presence of hexagonal $MoSi_2$, SiC, and $SiO_2$; this suggests that their volume fractions are low (<5 vol%), because the sensitivity limit of XRD is generally about 5 vol% (Ref 20).

Transmission electron microscopy studies further confirmed the complex phase constitution in the as-deposited RPS $MoSi_2$ (Fig. 3). It exhibits a homogeneous equiaxed grain morphology with a fine grain size in the range of 0.1 to 0.4 μm. The equiaxed

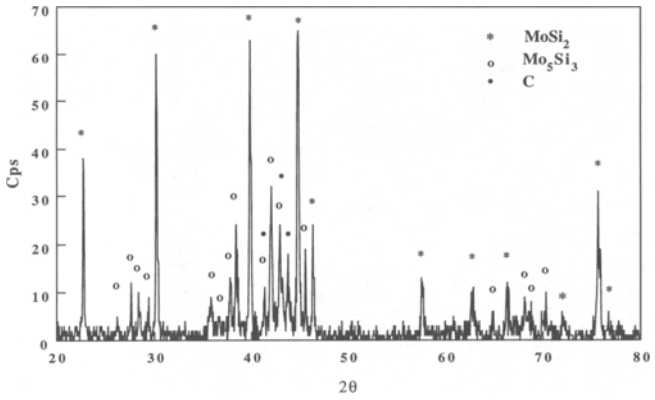


**Fig. 2** X-ray diffraction pattern and phase constitution of the as-deposited $MoSi_2$


**Fig. 3** TEM micrograph of the $MoSi_2$ matrix

grain morphology and fine grain size range are typical of plasma-sprayed $MoSi_2$ (Ref 12, 14-18). The $Mo_5Si_3$ phase with a plate morphology is frequently observed adjacent to the $MoSi_2$ phase. The platelike $Mo_5Si_3$ phase and the $MoSi_2$ phase form a eutectic microstructure, as shown in Fig. 4(a). The thickness of the $Mo_5Si_3$ phase is about 0.35 µm. Some $Mo_5Si_3$ phase is also observed as particles dispersed within the $MoSi_2$ matrix. The TEM observation of a large fraction of $Mo_5Si_3$ phase in the as-deposited RPS $MoSi_2$ is consistent with the bulk XRD results. Moreover, TEM observations also revealed SiC and $SiO_2$ phases in the as-deposited RPS $MoSi_2$, although these phases could not be detected by XRD analysis. For example, Fig. 4(b) shows an approximately 1 µm β-SiC particle that was formed at the splat boundary in the as-deposited RPS $MoSi_2$. In related studies, $SiO_2$ particles were also observed along the splat boundaries (Ref 11, 19). In the next section, the interactions of the $MoSi_2$ particles with the reactive gas and the plasma jet stream will be analyzed and used to explain the microstructural observations described here.

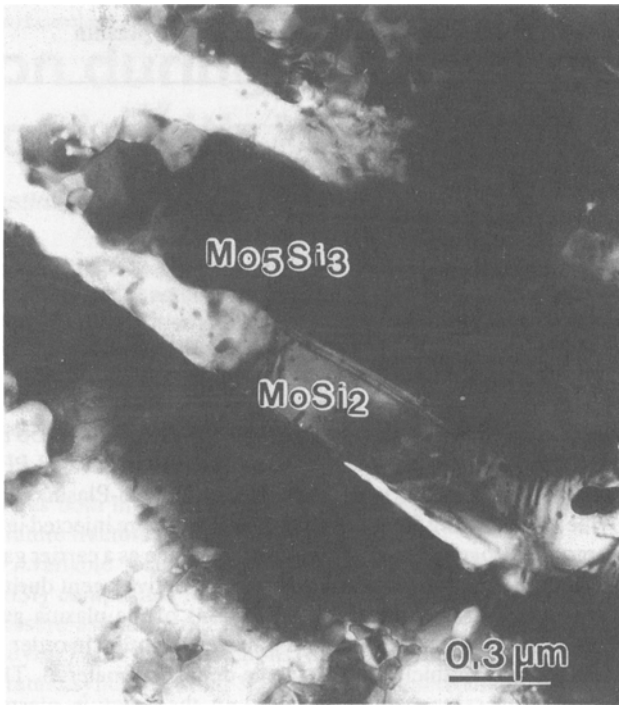


**(a)**

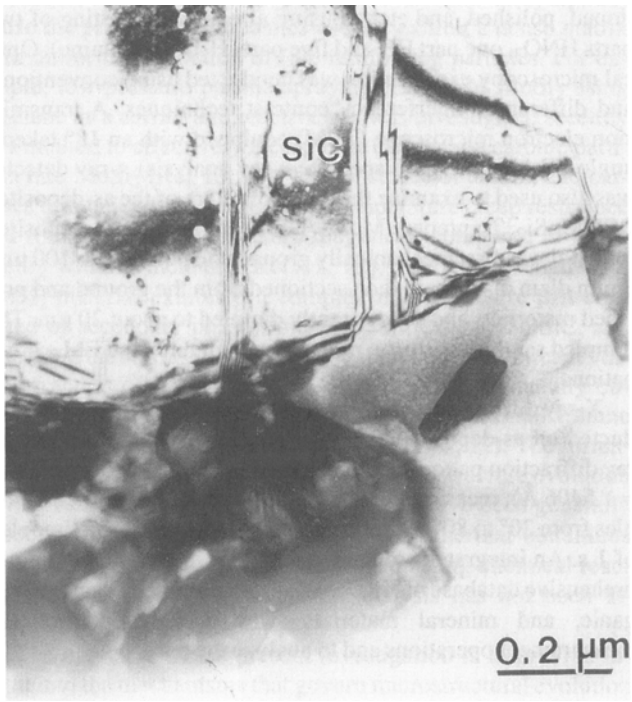


**(b)**

**Fig. 4** Typical lamellar $Mo_5Si_3$-$MoSi_2$ eutectic microstructure in the as-deposited $MoSi_2$. (b) A β-SiC particle in the as-deposited $MoSi_2$

## 4. Discussion

Different processes occur simultaneously during reactive plasma spraying. For example, the high temperature of the plasma gas jet may promote the dissociation and the subsequent

reactions of the methane gas. The interactions of the $MoSi_2$ powder particles with the plasma gas jet usually follow three mechanisms. First, $MoSi_2$ particles are accelerated or decelerated in the high-velocity plasma gas jet as a result of momentum interactions with the dynamic and highly heterogeneous plasma gas jet (Ref 4, 5, 21-23). Second, the extremely high-temperature plasma gas jet causes extensive heat transfer at interfaces between the $MoSi_2$ particles and the plasma gas, leading to heating, melting, and vaporization of the $MoSi_2$ particles (Ref 4, 5, 21-23). Third, vaporization and chemical reactions between the $MoSi_2$ particles and the plasma gas environment may lead to the formation of new phases (e.g., $Mo_5Si_3$, SiC, etc.) in the as-deposited RPS $MoSi_2$. The vaporization and chemical reactions are all strongly influenced by the dynamic and thermal behavior of the $MoSi_2$ particles along the thermal plasma jet.

Accordingly, in the following sections, the momentum and thermal interactions between the $MoSi_2$ particles and the plasma jet will be analyzed numerically. The phase transformations and chemical reactions will be analyzed on the basis of thermodynamic and kinetic considerations. These results will be correlated with the experimental observations.

## 4.1 *$MoSi_2$ Particle Behavior in the Thermal Plasma Jet*

### 4.1.1 Momentum Interactions between Particles and the Thermal Plasma Jet

Thermal plasma jets are generally characterized by high velocities (300 to 1000 m/s) and high temperatures (10,000 to 15,000 K) (Ref 4, 5, 21-24). Thermal plasma jets are also highly heterogeneous systems with large velocity and temperature variations. As a result, a thermal plasma provides extremely high accelerating or decelerating drag forces and heating or cooling rates for the $MoSi_2$ powder particles that are injected into it, depending on their relative velocity and temperature. Momentum interactions between the particles and the plasma gas ultimately govern the resultant particle motion and the ensuing thermal behavior. The acceleration and deceleration of a spherical particle in a viscous steady fluid is usually described by Newton's second law (Ref 4, 5, 22, 25), which (neglecting radial and angular velocity components) is given as:

$$V_d \rho_d \frac{dv_d}{dt} = A_d C_{drag}\, \rho_g |v_g - v_d|(v_g - v_d) \qquad \text{(Eq 1)}$$

where $\rho_d$ and $\rho_g$ are the densities of the powder particle and plasma gas, respectively; $V_d$ and $A_d$ are the volume and surface area of the particle, respectively; $v_d$ and $v_g$ are the velocities of the particle and plasma gas, respectively; $C_{drag}$ is the drag coefficient; and $t$ is time.

For the small-size (approximately 10 to 100 μm diameter) particles typically used in the plasma spraying, the steady-state drag coefficients can be determined by a form proposed by White (Ref 4, 5, 25):

$$C_{drag} = \frac{24}{Re} + \frac{6}{1+\sqrt{Re}} + 4$$

for $Re < 100$. $Re$ is the Reynolds number of the particle, defined as $Re = d\rho_g|v_g - v_d|/\mu_g$, where $d$ is the diameter of the particle and $\mu_g$ is the dynamic viscosity of the plasma gas. This drag coefficient, however, requires some modification because of factors that can influence the dynamic interaction between the particles and the thermal plasma gas. As suggested by Pfender et al. (Ref 5, 25-27), these factors include modified viscous drag due to strongly varying plasma properties, thermophoresis, noncontinuum effects, Basset history term, turbulent dispersion, particle shapes, vaporization, and particle charging. Many of these factors are important only when particle diameter is smaller than 10 μm (Ref 5, 25). Because the $MoSi_2$ powder size is in the range of 10 to 44 μm during the present plasma spraying, the drag coefficient will be affected only by the modified viscous drag and vaporization factors. The modified viscous drag and vaporization factors are $(\rho_g\mu_g/\rho_2\mu_w)^{-0.45}$ and $1 + C_p(T_g - T_W)/\Delta H_{vap}$ (Ref 5, 25-27), respectively. The subscripts g and w correspond to the plasma gas and the particle/gas interface, respectively; $C_p$ is the specific heat of the particle; $T$ is the temperature; and $\Delta H_{vap}$ is the heat of vaporization. Incorporating these factors, the drag coefficient is described as:

$$C_{drag} = \left(\frac{24}{Re} + \frac{6}{1+\sqrt{Re}} + 4\right)\left(\frac{\rho_g\mu_g}{\rho_w\mu_w}\right)^{-0.45}\left(1 + \frac{C_p(T_g - T_W)}{\Delta H_{vap}}\right) \qquad \text{(Eq 2)}$$

Equations 1 and 2, the physical properties of $MoSi_2$ listed in Table 2 (Ref 28), and the gas velocities determined on the basis of measurements and numerical analysis previously reported (Ref 4, 5, 21-23, 26) were used to calculate the particle velocities as a function of particle size and flight distance. The calculated results for the $MoSi_2$ particles are shown in Fig. 5, where it is observed that small particles (i.e., 15 to 25 μm) are accelerated to a maximum velocity in a short period of time, followed by a rapid deceleration. In contrast, the velocity profile of a large particle (i.e., 45 μm) exhibits only gradual changes. These results are consistent with numerical calculations and experimental measurements reported previously (Ref 4, 5, 21-23, 29).

### 4.1.2 Thermal Interactions between Particles and the Thermal Plasma Jet

During the motion of powder particles, thermal energy is transferred from the high-temperature plasma gas jet via the combined effects of convection and radiation. On the basis of a relatively high thermal conductivity for $MoSi_2$ (30 to 40 W/m · K at 1000 °C) (Ref 6, 7) and the powder size distribution used

**Table 2 Physical properties of $MoSi_2$**

| Parameter | Value |
|---|---|
| Density (ρ), kg/m$^3$ | 6310 |
| Heat capacity ($C_p$), J/kg · K | $67.8 \times 10^{-3}\,T - 6.6 \times 10^6\,T^{-2}$ |
| Melting temperature ($T_m$, K | 2303 |
| Boiling temperature ($T_b$)(a), K | 4000 |
| Latent heat of fusion ($\Delta H_f$), J/kg | $3.06 \times 10^5$ |
| Heat of vaporization ($\Delta H_{vap}$)(a), J/kg | $9.04 \times 10^6$ |

(a) Estimated. Source. Ref 28

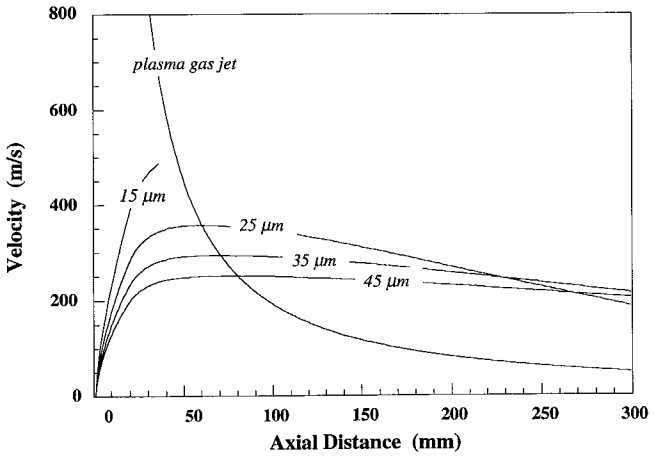


**Fig. 5** Calculated velocity profiles for $MoSi_2$ particles of different size along the plasma jet. The velocity profile for the 15 μm particulate is terminated after 40 mm due to complete vaporization.

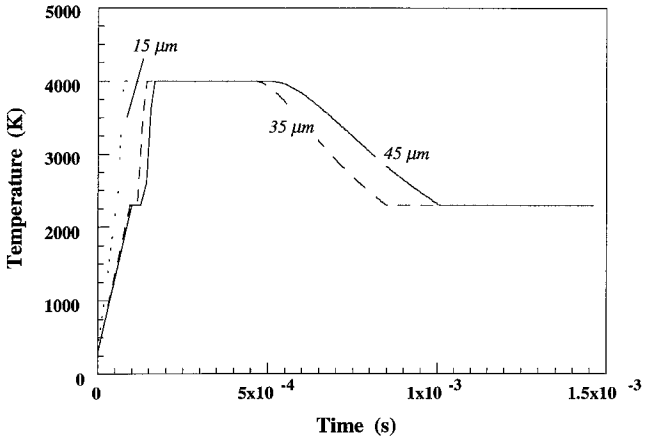


**Fig. 6** Calculated temperature profiles for $MoSi_2$ particles of different size as a function of time along the plasma jet

herein, it is reasonable to assume that the temperature distribution inside the particle (spherical) is homogeneous or Newtonian. Accordingly, under Newtonian conditions, an energy balance between the thermal energy of a particle and that transferred from the plasma gas jet leads to Ref 4, 5, 26):

$$\rho_d V_d C_d \frac{dT_d}{dt} = h(T_g - T_d)A_d + \varepsilon\sigma(T_g^4 - T_d^4)A_d \qquad \text{(Eq 3)}$$

where $h$ is the convection heat-transfer coefficient; $T_g$ and $T_d$ are the temperatures of the plasma gas and particle, respectively; $\sigma$ is the Stephen-Boltzmann constant; and $\varepsilon$ is the emissivity of the surface (Ref 30). The convection heat-transfer coefficient, $h$, estimated from the Ranz-Marstall correlation (Ref 4, 5, 26) incorporating the modified viscous drag and vaporization factors, is

$$h = \frac{K_g}{d}(2 + 0.6\sqrt{Re}^3\sqrt{Pr}\left(\frac{\rho_g\mu_g}{\rho_w\mu_w}\right)^{0.6}\left(\frac{C_{pg}}{C_{pw}}\right)^{0.38}\left(1 + \frac{C_p(T_g - T_W)}{\Delta H_{vap}}\right) \qquad \text{(Eq 4)}$$

where $K_g$ is the thermal conductivity of the gas, and $Pr$ is the Prandtl number of the plasma gas as defined by $Pr = C_{pg}\mu_g/K_g$ (Ref 30), where $C_{pg}$ is the specific heat of the plasma gas. For $MoSi_2$ particles, melting or solidification and vaporization of the particles must also be considered in the thermal analysis. Accordingly, during melting or solidification, the thermal energy changes inside a particle can be quantified by the changes in liquid fraction, $f_l$, according to:

$$\Delta H_f \rho_d V_d \frac{df_l}{dt} = h(T_g - T_m)A_d + \varepsilon\sigma(T_g^4 - T_m^4)A_d \qquad \text{(Eq 5)}$$

where $\Delta H_f$ is the latent heat of fusion and $T_m$ is the melting temperature of the particle. Similarly, during vaporization, the thermal energy changes inside a particle can be characterized by a vaporization factor, $f_{evp}$:

$$\Delta H_{vap}\rho_d V_d \frac{df_{evp}}{dt} = h(T_g - T_b)A_d + \varepsilon\sigma(T_g^4 - T_b^4)A_d \qquad \text{(Eq 6)}$$

where $T_b$ is the boiling temperature of the particle.

Using Eq 3 to 6 and the physical properties of $MoSi_2$ (Table 2), the thermal history of the particles along the plasma jet can be calculated as a function of flight distance or dwell time. Figure 6 shows the calculated temperature profile for $MoSi_2$ particles of different size along the plasma jet. The results reveal that the injected $MoSi_2$ particles experience several distinct stages. First, all particles are heated to the melting temperature and, subsequently, to the boiling temperature at extremely high rates. Second, extensive vaporization occurs when the temperature of the particles reaches the boiling point. Cooling of the particles begins at the moment when the temperature of the plasma gas is lower than that of the particles. Accordingly, the temperature of the $MoSi_2$ particles decreases by releasing thermal energy to the surrounding plasma gas. The cooling rates, shown in Fig. 6, are significantly slower than the heating rates.

## 4.2 *Vaporization of $MoSi_2$ in the Plasma Jet*

As shown in Fig. 6, the $MoSi_2$ particles experience a dwell time in the range of $2 \times 10^{-4}$ to $3 \times 10^{-4}$ at their boiling temperature. Consequently, extensive vaporization is expected. The vaporization of $MoSi_2$, however, may not be a homogeneous process because of a significant difference in the physical properties of molybdenum and silicon. For example, the boiling temperature of pure molybdenum is 4912 K, whereas that of pure silicon is 3540 K (Ref 28). This corresponds to a difference of 1372 K in boiling temperature. Hence, vaporization of silicon is expected to be much more severe than that of molybdenum under similar high-temperature conditions. As a result, a surface region where silicon concentration is relatively lower than that of the interior may exist. From the molybdenum-silicon phase diagram (Fig. 7), a $Mo_5Si_3$-$MoSi_2$ eutectic microstructure can be formed in the corresponding silicon-depleted surface region. Such a microstructure is shown in Fig. 4. It is worth noting that extensive vaporization of silicon should not occur only in the

**Table 3 Chemical reactions that may occur as a function of temperature during plasma spraying of $MoSi_2$ using methane as a reactive gas**

| Temperature | Reaction |
|---|---|
| $T > 1750$ K | $3\,CH_4\,(g) + SiO_2\,(s) = SiC\,(s) + 2CO\,(g) + 6H_2\,(g)$ |
| | $SiO_2\,(s) + 3C\,(s) = SiC\,(s) + 2CO\,(g)$ |
| | $6\,MoSi_2\,(s) + 3SiO_2\,(s) + 14C\,(s) = Mo_5Si_3\,(s) + 11SiC\,(s) + SiO\,(g) + 2CO\,(g) + MoO_3\,(g)$ |
| $T < 1750$ K | $5MoSi_2\,(s) + 7C\,(s) = Mo_5Si_3\,(s) + 7SiC\,(s)$ |
| | $5MoSi_2\,(s) + 7O_2\,(g) = Mo_5Si_3\,(s) + 7SiO_2\,(s)$ |

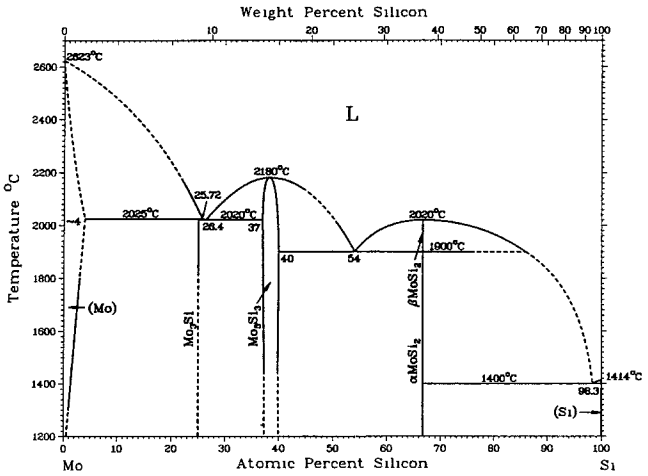


**Fig. 7** Molybdenum-silicon phase diagram. Source: Ref 31

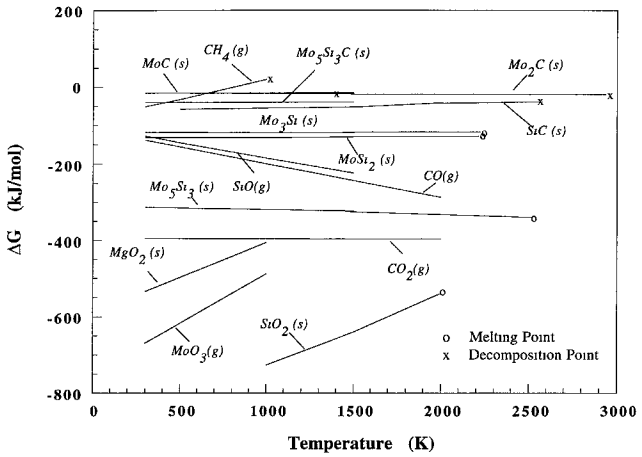


**Fig. 8** Gibbs free energy of the phases that may be present during plasma spraying of $MoSi_2$ using 100% methane as a reactive gas. Source: Ref 28

present RPS process, but also in any plasma spraying of $MoSi_2$ performed under conditions of high temperature and low gas partial pressure, leading to formation of the $Mo_5Si_3$-$MoSi_2$ eutectic microstructure. This suggestion is in agreement with the results of Tiwari et al. (Ref 18), Castro et al. (Ref 12), and Lawrynowicz et al. (Ref 11), who observed a $Mo_5Si_3$-$MoSi_2$ eutectic microstructure during plasma spraying of monolithic and ceramic-reinforced $MoSi_2$. Further confirmation of $Mo_5Si_3$ formation due to silicon evaporation at high temperatures (Ref 32) indicated that evaporation of silicon from $MoSi_2$ became significant above 1600 °C and that $MoSi_2$ subsequently converted to $Mo_5Si_3$ in the surface region.

## 4.3 *Chemical Reaction Thermodynamics*

Thermodynamic analysis can serve as a guideline to establish which phases are present as a function of temperature during RPS. In the present reactive plasma spraying of $MoSi_2$, the reactants include Ar (g), $H_2$ (g), $CH_4$ (g), $O_2$ (g), (contamination in the chamber), $MoSi_2$ (s), and $SiO_2$ (s) (surface layer). Under the high-temperature conditions (Fig. 5) provided by the thermal plasma jet, chemical reactions among $CH_5$, $O_2$, $MoSi_2$, and $SiO_2$ and phase transformations (i.e., vaporization) may lead to the formation of new phases. A detailed thermodynamic analysis for all the species that may form is needed to determine the final products.

Accordingly, the Gibbs free energy of formation for all the possible species in the reactive plasma environment is plotted in Fig. 8 as a function of temperature. Several important points are noted. First, methane is dissociated to C (g), H (g), $C_2H$ (g), $C_2H_2$ (g), and other hydrocarbons simultaneously above 700 K. The presence of an ion plasma can further accelerate the methane dissociation, which has been demonstrated to be a critical process during plasma carburization (Ref 33). As a result, immediate dissociation of methane is expected once it is injected into the extremely high-temperature (10,000 to 15,000 K) plasma gas jet. Consequently, a high concentration of elemental carbon will be present in the high-temperature plasma gas jet. Second, $SiO_2$ is the most stable phase below 1750 K. This result suggests that any reaction of the $MoSi_2$ particles with oxygen will lead to the formation of $SiO_2$. This may explain the existence of the $SiO_2$ at the splat boundaries in the as-deposited RPS $MoSi_2$ (Ref 11). At higher temperatures (>1750 K), silica will dissociate into SiO (g), Si (g), and O (g) (Ref 34-36). Third, carbides such as SiC, MoC, $MoC_2$, and $Mo_5Si_3C$ are not as stable as the silicides and oxides. This prediction is in agreement with the small amount of carbides observed in the as-deposited RPS $MoSi_2$. Fourth, $Mo_5Si_3$ is the most stable phase among the three molybdenum-silicon phases ($MoSi_2$, $Mo_5Si_3$, and $Mo_3Si$). Thus, if $MoSi_2$ loses silicon to the environment, via oxidation or vaporization as previously discussed. $Mo_5Si_3$ is likely to be formed. This may explain why both x-ray and TEM analysis revealed a high volume fraction of $Mo_5Si_3$ phase in the as-deposited RPS $MoSi_2$.

It is also important to consider the possible chemical reactions that might occur on the basis of the Gibbs free energy analyses. In Table 3, the critical chemical reactions that might

occur under the present thermal plasma conditions are listed as a function of temperature. Above 1750 K, reactions associated with silica lead to the formation of solid $Mo_5Si_3$ and SiC, plus other gaseous products. Below 1750 K, $MoSi_2$ may react with carbon or oxygen to form a solid $Mo_5Si_3$, $SiO_2$, and SiC. It is important to note that the $Mo_5Si_3$ phase forms at all temperatures. Once formed, $Mo_5Si_3$ is very stable. It will not react with carbon to form SiC according to:

$$3Mo_5Si_3\,(s) + 4C\,(s) = 5Mo_3Si\,(s) + 4SiC\,(s) \qquad \text{(Eq 7)}$$

because this reaction has a positive change of Gibbs free energy (e.g., $\Delta G$ = 183 kJ/mol at 1500 K) and thus may be an important reason for the low volume fraction of SiC observed in the as-deposited material. It should be mentioned that the present thermodynamic analyses were based on the equilibrium conditions. Accordingly, stable phases under equilibrium conditions may not occur in a highly heterogeneous condition usually present during plasma spraying. The corresponding heterogeneous reactions and phase transformations must be considered with their kinetics during plasma spraying.

## 4.4 *Microstructure Evolution during Reactive Plasma Spraying of $MoSi_2$*

Under the high-temperature and high-velocity conditions provided by the thermal plasma jet, any chemical reactions must be analyzed in conjunction with the reaction kinetics and thermal history experienced by the $MoSi_2$ particles. As discussed in the previous section, the thermal history of the powder along the plasma jet can be divided into several stages: rapid heating, extensive vaporization, and cooling (Fig. 6). No significant evaporation and chemical interactions occur in the rapid heating stage due to an extremely short time ($1 \times 10^{-4}$ to $3 \times 10^{-4}$ s) spent in this stage, whereas during the subsequent vaporization stage, extensive surface vaporization leads to a mass loss from the particles to the surrounding environment. As a result, although adsorption of the gaseous species onto the surface of the particles is possible, extensive vaporization of the surface layer will put these species back into the surrounding environment. As a result, no chemical reactions occur in this stage. The mass loss from the particles will continue by evaporation even when the temperature is lower than the boiling point of the material (Ref 5, 29), until the vapor pressure is lower than that of the surrounding atmosphere.

Once the mass loss from evaporation is reduced, carbon (dissociated from $CH_4$) and oxygen will deposit onto the surface of the $MoSi_2$ particle. Three processes may then occur: (1) adsorption of the carbon or oxygen onto the surface of the $MoSi_2$ particles, (2) diffusion of carbon or oxygen from the surface toward the interior, and (3) chemical reactions with the matrix $MoSi_2$ to form new phases. These processes are strongly influenced by factors such as the partial pressure of carbon or oxygen, temperature, and reaction thermodynamics and kinetics. The effects will be discussed in detail as a function of temperature ($T$) experienced by the $MoSi_2$ particles. It is necessary to define the temperatures that are used in the following discussion. $T_{SiC}$ is the temperature at which SiC sublimes, and $T_{Mo_5Si_3}$ is the melting temperature of the $Mo_5Si_3$ phase.

### 4.1.1 $T > T_{SiC}$ (= 2818 K) (Ref 31)

In this temperature range, no chemical reactions are expected based on thermodynamic analysis (Fig. 8). Accordingly, deposition of carbon and oxygen and their subsequent diffusion into the $MoSi_2$ particles will occur. The rate of deposition of carbon and oxygen is related to their partial pressures and deposition temperatures (Ref 37). The rate for diffusion is determined by their diffusivities. Quantitative determination of the deposition and diffusion rates at high temperatures is difficult. Although the diffusion rate may be very high due to the high temperatures, the deposition rate may not be very high, because the species may evaporate back into the surrounding atmosphere. Moreover, any significant mass transport may be critically limited by a short time experienced by the particles ($1 \times 10^{-4}$ to $10 \times 10^{-4}$ s, Fig. 6) in the present temperature range.

### 4.4.2 $T_{SiC} > T > T_{Mo_5Si_3}$ (= 2543 K)

Silicon carbide forms by carbon reacting with silicon in this temperature range. Silicon carbide formation, however, may be limited for several reasons. First, as suggested by the previous thermodynamic analysis, the Gibbs free energy of SiC formation is low compared to other phases (Fig. 8). Second, the surface layer on the $MoSi_2$ particle may have a relatively low silicon content due to extensive vaporization. Accordingly, there will be insufficient silicon to react with carbon. Third, the extremely short time that the $MoSi_2$ particles are exposed in this temperature range, on the order of $10^{-4}$ s (Fig. 6), probably allows no chemical reactions to go to completion. As a result, it is almost impossible to form a significant amount of SiC in this temperature range.

### 4.4.3 $T < T_{Mo_5Si_3}$

The subsequent cooling of the $MoSi_2$ particles will lead to the nucleation and formation of the $Mo_5Si_3$ phase in the surface region as a result of several processes. First, the surface layer of the $MoSi_2$ particles will have a lower silicon concentration due to vaporization, leading to the formation of the eutectic $Mo_5Si_3$-$MoSi_2$ microstructure. Second, any chemical reactions that involve $MoSi_2$ will result in the formation of $Mo_5Si_3$ as a reaction product (Table 3). Moreover, the time in this temperature range is significantly longer than for the previous temperature ranges, further enhancing completion of the reaction. The combination of these effects can lead to the formation of a significant amount of $Mo_5Si_3$ phase in the surface layer. In addition, the $Mo_5Si_3$ phase may eventually form a surface layer that covers the $MoSi_2$ particle. It has been shown in previous sections that the $Mo_5Si_3$ phase is thermodynamically very stable (Fig. 8). Although deposition of carbon and oxygen continues in this temperature range, the existence of the $Mo_5Si_3$ surface layer may dramatically reduce their reaction with the interior $MoSi_2$, because carbon or oxygen must first diffuse through the solid $Mo_5Si_3$ phase. Consequently, it is possible that a $Mo_5Si_3$ surface layer can act as a protective layer against further reactions, similar to an alumina layer on aluminum that prevents further oxidation. On the basis of this analysis, it is suggested that a substantial amount of $Mo_5Si_3$ will be formed, whereas the amount of SiC will be insig-

nificant. Such suggestions are in agreement with experimental observations for the RPS $MoSi_2$.

Subsequent deposition of the $MoSi_2$ particles onto the substrate leads to the formation of a dense deposit. In addition to the dramatic heat exchange among the particles, plasma gas jet, and substrate (Ref 38), the semisolid $MoSi_2$ particles experience a significant amount of deformation as a result of their high dynamic energy upon impact. As a result, a layer structure of deformed splats will form. Moreover, due to the existence of $Mo_5Si_3$ phase in the surface layer, the unreacted carbon and the newly formed SiC or $SiO_2$ particles will segregate along the splat boundaries. In related investigations, Castro et al. (Ref 10) observed that amorphous carbon particulates were concentrated along the splat boundaries in RPS $MoSi_2$ using Ar-10$CH_4$, and Lawrynowicz et al. (Ref 11) observed that $SiO_2$ was also concentrated along the splat boundaries. These experimental observations provide support to the proposed microstructural evolution mechanism.

## 5. Conclusions

The as-deposited RPS $MoSi_2$ using 100% methane exhibited a nearly fully dense, multilayered microstructure. X-ray diffraction revealed a complex phase constitution in the as-deposited $MoSi_2$. In addition to the $MoSi_2$ matrix, significant amounts of $Mo_5Si_3$ and elemental carbon were observed. Examination by TEM revealed that the $Mo_5Si_3$ and $MoSi_2$ phases form a lamella eutectic microstructure. Low amounts of SiC and $SiO_2$ were observed.

Analysis of the Gibbs free energy of formation for the possible species in the presence of $CH_4$, $O_2$, $MoSi_2$, and $SiO_2$ under the plasma environment suggested that: (1) Methane is dissociated to C, H, $C_2H$, $C_2H_2$, and other hydrocarbons at high temperatures; (2) $SiO_2$ is the most stable phase below 1750 K, whereas SiC and other carbides such as MoC, $MoC_2$, and $Mo_5Si_3C$ are the least stable; (3) $Mo_5Si_3$ is the most stable phase among the three molybdenum-silicon phases ($MoSi_2$, $Mo_5Si_3$, and $Mo_3Si$); and (4) further reaction of $Mo_5Si_3$ with carbon to form SiC is impossible.

Analysis of the thermal behavior suggested that $MoSi_2$ particles experience extensive vaporization. Heterogeneous vaporization of the $MoSi_2$ leads to a silicon-depleted surface layer, which results in the subsequent formation of the eutectic $Mo_5Si_3$-$MoSi_2$.

Thermodynamics predicted a relatively large volume fraction of $Mo_5Si_3$ and a small amount of SiC in the as-deposited RPS $MoSi_2$. It was also suggested that the existence of the $Mo_5Si_3$ surface layer dramatically reduces chemical reactions with the interior $MoSi_2$, because carbon or oxygen must first diffuse through the $Mo_5Si_3$ layer.

### Acknowledgments

Financial support from the Schott Glaswerke under the guidance of Dr. J. Disam is gratefully acknowledged. The authors would also like to thank Mr. D. Lawrynowicz for many useful discussions. EJL wishes to acknowledge the Army Research Office (DAAH04-95-1-042 for support.

### References

1. R.W. Smith, Reactive Plasma Spray Forming for Advanced Materials Synthesis, *Powder Metall. Int.*, Vol 25, 1993, p 9-16
2. Z.Z. Mutasim and R.W. Smith, Reactive Plasma Spray Forming, *Thermal Spray Coatings: Properties, Processes, and Applications,* T.F. Bernecki, Ed., ASM International, 1992, p 273-279
3. K. Murakami, A. Yoshimoto, T. Okamoto, and Y. Miyamoto, Plasma Spray Synthesis of Composite Materials with Fine Titanium Carbide Particles, *Mater. Sci. Eng.*, Vol A160, 1993, p 137-142
4. D. Apelian, M. Paliwal, R.W. Smith, and W.F. Schilling, Melting and Solidification in Plasma Spray Deposition—Phenomenological Review, *Int. Met. Rev.*, Vol 28, 1983, p 271-294
5. E. Pfender, Plasma Jet Behavior and Modeling Associated with the Plasma Process, *Thin Solid Films,* Vol 238, 1994, p 228-242
6. Y.-L. Jeng and E.J. Lavernia, Processing of Molybdenum Disilicide, *J. Mater. Sci.*, Vol 29, 1994, p 2557-1571
7. A.K. Vasudevan and J.J. Petrovic, A Comparative Overview of $MoSi_2$ Composites, *Mater. Sci. Eng.*, Vol A155, 1992, p 1-17
8. J. Winnerl, Silicides for High Density Memory and Logic Circuits, *Semicond. Int.*, Vol 17, 1994, p 81-86
9. M.J. Maloney and R.J. Hecht, Development of Continuous-Fiber-Reinforced $MoSi_2$-Base Composites, *Mater. Sci. Eng.*, Vol A155, 1992, p 19-32
10. R.G. Castro, H. Kung, and P.W. Stanek, Reactive Plasma Spraying of $MoSi_2$ Using an Ar-10%CH4 Powder Carrier Gas, *Mater. Sci. Eng.*, Vol A185, 1994, p 65-70
11. D.E. Lawrynowicz, J. Wolfenstine, E.J. Lavernia, S.R. Nutt, D.E. Bailey, A. Sickinger, and A.M. Hirt, Reactive Synthesis and Characterization of $MoSi_2$/SiC Using Low-Pressure Plasma Deposition and 100% Methane, *Scr. Metall. Mater.*, Vol 32, 1995, p 689-693
12. R.G. Castro, J.R. Hellmann, A.E. Segall, and D.L. Shelleman, Fabrication and Testing of Plasma-Sprayed Formed $MoSi_2$ and $MoSi_2$ Composite Tubes, *Mater. Res. Soc. Symp. Proc.*, Vol 322, 1994, p 81-87
13. X. Liang, J.C. Earthman, J. Wolfenstine, and E.J. Lavernia, A Comparison of Techniques for Determining the Volume Fraction of Particulates in Metal Matrix Composites, *Mater. Char.*, Vol 28, 1992, p 173-178
14. R.G. Castro, R.W. Smith, A.D. Rollett, and P.W. Stanek, Ductile Phase Toughening of $MoSi_2$ by Low Pressure Plasma Spraying, *Mater. Sci. Eng.*, Vol A155, 1992, p 101-107
15. Y.-L. Jeng, E.J. Lavernia, J. Wolfenstine, D.E. Bailey, and A. Sickinger, Creep Behavior of Plasma-Sprayed SiC-Reinforced $MoSi_2$, *Scr. Metall. Mater.*, Vol 29, 1993, p 107-111
16. Y.-L. Jeng, J. Wolfenstine, E.J. Lavernia, D.E. Bailey, and A. Sickinger, Low Pressure Plasma Deposition of SiC-Reinforced $MoSi_2$, *Scr. Metall. Mater.*, Vol 28, 1993, p 453-458
17. S. Sampath and H Herman, Plasma Spray Forming Metals, Intermetallics, and Composites, *J. Met.*, Vol 45, 1993, p 42-49
18. R. Tiwari, H. Herman, and S. Sampath, Vacuum Plasma Spraying of $MoSi_2$ and Its Composites, *Mater. Sci. Eng.*, Vol A155, 1992, p 95-100
19. D.E. Lawrynowicz, J. Wolfenstine, S.R. Nutt, and E.J. Lavernia, Synthesis and Properties of $MoSi_2$/SiC Processed by Low-Pressure Plasma Co-Injection and Deposition, *Mater. Res. Soc., Symp. Proc.*, Vol 322, 1994, p 132-147
20. B.D. Cullity, *Elements of X-ray Diffraction,* 2nd ed., Addison-Wesley, 1978
21. A.H. Dilawari, and J. Szekely, Some Perspectives on the Modeling of Plasma Jets, *Plasma Chem. Plasma Process.*, Vol 7, 1987, p 317-339
22. D.J. Varacalle, An Analytical Methodology to Predict the Coating Characteristic of Plasma-Sprayed Ceramic Powders, *Thermal Spray Research and Applications,* T.F. Bernecki, Ed., ASM International, 1990, p 271-283
23. D.K. Das and R. Sivakumar, Modeling of the Temperature and the Velocity of Ceramic Powder Particles in a Plasma Flame, *Acta Metall. Mater.*, Vol 38, 1990, p 2187-2192

24. A. Sickinger and E. Muehlberger, Advanced Low Pressure Plasma Application in Powder Metallurgy, *Powder Metall. Int.*, Vol 24, 1992, p 91-94
25. Y.C. Lee, Y.P. Chyou, and E. Pfender, Particle Dynamics and Particle Heat and Mass Transfer in Thermal Plasma. Part II. Particle Heat and Mass Transfer in Thermal Plasma, *Plasma Chem. Plasma Process.*, Vol 5, 1985, p 391-414
26. Y.C. Lee and E. Pfender, Particle Dynamics and Particle Heat and Mass Transfer in Thermal Plasma. Part III. Thermal Plasma Jet Reactors and Multiparticle Injection, *Plasma Chem. Plasma Process.*, Vol 7, 1985, p 1-17
27. E. Pfender and Y.C. Lee, Particle Dynamics and Particle Heat and Mass Transfer in Thermal Plasma. Part I. The Motion of a Single Particle without Thermal Effects, *Plasma Chem. Plasma Process.*, Vol 5, 1985, p 211-237
28. C.J. Smithell, *Smithells Metals Reference Book,* 6th ed., Butterworths, 1983
29. X. Chen, T.P. Chyou, Y.C. Lee, and E. Pfender, Heat Transfer to a Particle under Plasma Conditions with Vapor Contamination from the Particle, *Plasma Chem. Plasma Process.*, Vol 5, 1985, p 119-141
30. E.P. Incorpera, *Introduction to Heat Transfer,* John Wiley & Sons, 1985
31. T.B. Massalski, H. Okamoto, P.R. Subramanian, and L. Kacprzak, *Binary Alloy Phase Diagrams,* ASM International, 1990
32. G.B. Cherniack and A.G. Elliot, High Temperature Behavior of $MoSi_2$ and $Mo_5Si_3$, *J. Am. Ceram. Soc.*, Vol 47, 1964, p 136-141
33. W.L. Grube and J.G. Gay, High Rate Carburizing in a Glow-Discharge Methane Plasma, *Metall. Trans. A.*, Vol 9A, 1978, p 1421-1429
34 Y. Chang and E. Pfender, Thermochemistry of Thermal Plasma Chemical Reactions. Part I. General Rules for the Prediction of Products, *Plasma Chem. Plasma Process.*, Vol 7, 1987, p 275-297
35. Y. Chang, R.M. Young, and E. Pfender, Thermochemistry of Thermal Plasma Chemical Reactions. Part II. A Survey of Synthesis Routes for Silicon Nitride Production, *Plasma Chem. Plasma Process.*, Vol 7, 1987, p 299-316
36. P.R. Taylor and S.A. Pirzada, Ceramic Carbide Powder Synthesis in a Non-Transferred Arc Thermal Plasma Flow Reactor, *Mater. Manuf. Process.*, Vol 8, 1993, p 501-517
37. H. Liu, X. Zeng, and E.J. Lavernia, Processing Maps for Reactive Atomization and Deposition Processing, *Scr. Metall. Mater.*, Vol 29, 1993, p 1341-1344
38. X. Liang and E J. Lavernia, Evolution of Interaction Domain Microstructure during Spray Deposition, *Metall. Mater. Trans. A*, Vol 25A, 1994, p 2341-2355